Abundant grain boundaries activate highly efficient lithium ion transportation in high rate $Li_4Ti_5O_{12}$ compact microspheres

Ma, Jiaming; Wei, Yinping; Gan, Lin; Wang, Chao; Xia, Heyi; Lv, Wei; Li, Jia; Li, Baohua; Yang, Quan Hong; Kang, Feiyu

DOI
10.1039/c8ta10072a

Publication date
2019

Document Version
Accepted author manuscript

Published in
Journal of Materials Chemistry A

Abundant grain boundaries activate highly efficient lithium ion transportation in high rate $Li_4Ti_5O_{12}$ compact microspheres

Jiaming Ma [a, b], Yinping Wei [a], Lin Gan [a], Chao Wang [c], Heyi Xia [a, b], Wei Lv [a], Jia Li [a], Baohua Li[a], Quan-Hong Yang[d], Feiyu Kang [a, b] and Yan-Bing He [a,*]

[a] Engineering Laboratory for the Next Generation Power and Energy Storage Batteries, Graduate School at Shenzhen, Tsinghua University, Shenzhen 518055, PR China.

[b] Laboratory of Advanced Materials, Department of Materials Science and Engineering, Tsinghua University, Beijing 100084, PR China.

[c] Department of Radiation Science and Technology, Delft University of Technology, Mekelweg 15, Delft 2629 JB, The Netherlands

[d] Nanoyang Group, School of Chemical Engineering and Technology, Tianjin University, Tianjin, China

* Corresponding author. E-mail address: he.yanbing@sz.tsinghua.edu.cn (Y.-B. He)

Abstract

It is a huge challenge for high tap density electrode to achieve high volumetric energy density but do not compromise the ionic transportation. Herein, we prepared compact LTO microspheres consist of densely packed primary nanoparticles. The real space distribution of lithium ions inside the compact LTO was revealed by using the scanning transmission electron microscopy with electron energy loss spectroscopy (STEM-EELS) to identify the function of grain boundaries for lithium ion transportation during lithiation. The as-prepared LTO microspheres possess a high tap density (1.23 g cm^{-3}) and an ultra-small specific surface area (2.40 m^2 g^{-1}). Impressively, the compact LTO microspheres present excellent electrochemical performance. At a high rate of 5 C, 10 C and 20 C, the LTO microspheres show specific capacity of 146.6, 138.2 and 111 mA h g^{-1}, respectively. The capacity retention still remains 97.8% at 5 C after 500 cycles. The STEM-EELS results present that the lithiation reaction of LTO are firstly initiated at grain boundaries during high rate lithiation process and then diffused to bulk area. The abundant grain boundaries in compact LTO microspheres can form a highly efficient conductive network to preferentially transport the ions, which contributes to high volumetric and gravimetric energy density simultaneously.

Keywords: Compact $Li_4Ti_5O_{12}$ secondary microspheres, High tap density, Ultra-small specific surface area, Remarkable performance, Grain boundaries

1. Introduction

Because of their relatively high energy density, lithium ion batteries (LIBs) have been developed rapidly to meet the growing market of electric vehicles (EVs) and hybrid electric vehicles (HEVs)[1-3]. The most common problems of LIBs are their poor safety, inferior rate and low temperature charging properties. As the most widely used conventional anode material, the commercial graphite suffers from poor and low temperature charging properties due to the lithium metal deposition and lithium dendrite formation on the graphite anode at these conditions. In addition, the solid electrolyte interphase (SEI) layers may be destroyed at large working current densities and high working temperature, which further causes serious safety problems[4-7]. Thus, great efforts were devoted to explore new anode materials for LIBs with excellent rate performance and low temperature charging performance.

Among the candidate anodes, spinel $Li_4Ti_5O_{12}$ (LTO) has been widely studied as a promising alternative anode material, due to its: i) excellent cycle performance because of its "zero-strain" property during lithiation/delithiation process[8, 9]; ii) high flat potential of 1.55 V, which avoids SEI formation and provides a great safety improvement[10, 11]. Nevertheless, a low electronic conductivity (10^{-13} S cm^{-1}) and Li^+ diffusion coefficient (10^{-9}-10^{-13} cm^2 s^{-1}) of LTO restrict its electrochemical performance, especially high rate performance[12-14]. Many approaches have been used to develop high rate LTO materials by improving its electron transfer and shortening the ion transport path. One common route to improve the electronic conductivity is surface coating, including carbon coating[15, 16] and oxide coating[17], which significantly increase the surface electronic conductivity of LTO. Meanwhile, it can also relief the gassing problem arising from the intrinsic reaction between LTO electrode and electrolyte[18]. What's more, to further improve the electron transfer, combining LTO

nanostructures with carbon conductive matrixes such as carbon fibers, graphene, carbon nanotubes, etc. was also widely investigated[19-23].

The effective way to enhance the Li^+ diffusion coefficient is to construct the LTO materials with small size, such as nanoparticles[24], nanosheets[25, 26], nanofibers[27], nanoflowers[28], nanotubes[29], nanospheres[15], etc. These nano-sized LTO materials provide shortened transportation path for ions/electrons and increase electrode/electrolyte interface. The nano-sized LTO materials present excellent high rate and long cycling electrochemical performance. However, when the size of LTO materials decreases to nanoscale, their specific surface area increases greatly, leading to irreversible reactions with the electrolyte. Another non-negligible problem is that both nanoscale materials and the composites with carbon conductive matrixes suffer from a very low tap density which sacrifices the volumetric energy density. Therefore, it is a huge challenge to develop the LTO materials that combine high volumetric energy density meanwhile with a high power density and long cycle life[30]. This requires electrode materials with large tap densities, but barely compromising the charge transportation. Our group previously synthesized a compact LTO sub-microsphere consisting of densely packed nanocrystals with grain boundaries[31]. This material shows excellent electrochemical performance. Based on the electrochemical analysis, we proposed that the grain boundaries throughout the spheres may form 3D ionic transportation tunnel to achieve high electronic and ionic conductivity. However, the reaction mechanism is not yet clear, and there is lack of the real space observation of lithium ions transportation that is of great significance for understanding the detailed process of how grain boundaries transport the ions[32]. In addition, our prepared LTO sub-microsphere with diameter size of 500nm may be

not sufficient to reveal the ionic conductivity of grain boundaries. Therefore, it is essential to synthesis a compact LTO microspheres to observe the lithium ion transportation in real space. Furthermore, a visualized tool is also needed to investigate the lithium ion transportation mechanism in this densely packed material[33-35].

In this work, we fabricated compact secondary LTO microspheres consisting of densely packed primary nanoparticles with carbon coating by an in-situ growth. The as prepared LTO microspheres have a very small specific surface area (2.40 $m^2 g^{-1}$) and a high tap density (1.23 g cm^{-3}). The specific capacities of the LTO microspheres at 1, 5, 10 and 20 C are 162.4, 146.6, 138.2 and 111 mA h g^{-1}, respectively. The charge capacity still remains 97.8% at a high rate of 5 C after 500 cycles, showing excellent rate and cycling performance. The STEM-EELS results present that during high rate lithiation, the Li ions firstly gather around grain boundaries and then diffuse bulk LTO. The abundant grain boundaries of compact LTO microspheres are responsible for the high efficient lithium ion transportation. This work demonstrates that an exceptionally high rate performance can be combined with high tap density in LTO to achieve a large volumetric energy density and power density simultaneously.

Experimental Section

Synthesis of the $Li_4Ti_5O_{12}$ Secondary Microspheres

The compact LTO secondary microspheres were prepared as follows. First, 0.5 g of TiN nanopowders were dispersed in 28 ml of deionized(DI) water, then adding 16 ml of hydrogen peroxide(30%) and 6 ml of ammonia solution(25%-28%) into the mixing solution above.

After magnetic stirring for 0.5h, the mixing solution was gradually transformed into a transparent yellow solution of peroxo-titanium complex. After that, the solution containing 50 ml DI water and different ratio of ethanol (the ethanol proportion in the total solution was 40%, 50%, 60% and 70%) were added into the mixing solution. 5 minutes later, the obtained solution was stored in an oven at 80 ^{o}C for 4 hours for nucleation and growth of peroxo-titanium complex. Subsequently, 0.7 g lithium acetate and 0.11 g glucose were added into the precursor solution with magnetic stirring for 10 minutes. Then the solution was dried at 80 ^{o}C for 30 hours to obtain loose yellow powders. Finally, the powder was further annealed at 800 ^{o}C for 7 h in an Ar flow to obtain the final LTO (named as LTO-40% ethanol, LTO-50% ethanol, LTO-60% ethanol and LTO-70% ethanol).

Materials Characterization

The LTO microspheres compositions were characterized by X-ray diffraction (Rigaku D/max 2500/PC using Cu Kα radiation with λ = 1.5418 Å). The nitrogen adsorption/desorption isotherms were obtained at 77 K by using an automated adsorption apparatus (Micromeritics ASAP 2020). The surface area and pore size distribution was calculated based on the BET equation and density functional theory (DFT) methods. The tap density is measured by the GeoPyc1360 machine. Scanning electron microscopy (SEM) images was characterized by a field emission scanning electron microscope (HITACHI (SU8010)). High resolution transmission electron microscope (HRTEM) (TECNAIG2 F30) was also used at an accelerating voltage of 300 kV. The cross-section of LTO microspheres was obtained by model Leica EM RES 102 ion milling system. The Leica UC7 ultra-microtome was used to prepare the nanosheets of LTO microspheres for TEM

characterization. The carbon content was determined by a Netzsch STA 449F3 thermal analyzer under an air flow rate of 100 C min^{-1} from room temperature to 800 ^{o}C.

Electrochemical Measurements

The LTO electrode was fabricated by mixing 80 wt% as-prepared materials with 10 wt% conductive Super P and 10 wt% polyvinylidene fluoride (PVDF) dissolved in N-methyl-2-pyrrolidone (NMP), then the slurry was uniformly coated on a copper foil current collector (the LTO electrode loading is nearly about 2.0 mg cm^{-2} for the tested samples). The electrode was dried at 80 ^{o}C for 12 hours in a vacuum drying oven. The anode is metallic lithium and the 1M LiPF6 solution in ethylene carbonate (EC)/diethyl carbonate (DEC)/ethyl methyl carbonate (EMC) (volume ratio: 1:1:1) was used as the electrolyte. Microporous polyethylene (Celgard2500) served as the separator. Then the electrochemical characterization was performed using CR2032 coin half-cells. The half cells were galvanostatically cycled between 1.0 and 2.5 V (on a Land 2001A battery testing system) at different current densities (the current density of 1C corresponds to 175 mA g^{-1}) at room temperature. EIS was measured at half discharge state of electrode by a VMP3 multichannel electrochemical station in the frequency range from 10^{-2} to 10^{5} Hz. Cyclic voltammograms (CVs) were recorded using the same electrochemical workstation at a scan rate of 0.1 mV s^{-1} in the range of 1.0-2.5 V.

2. Results and Discussion

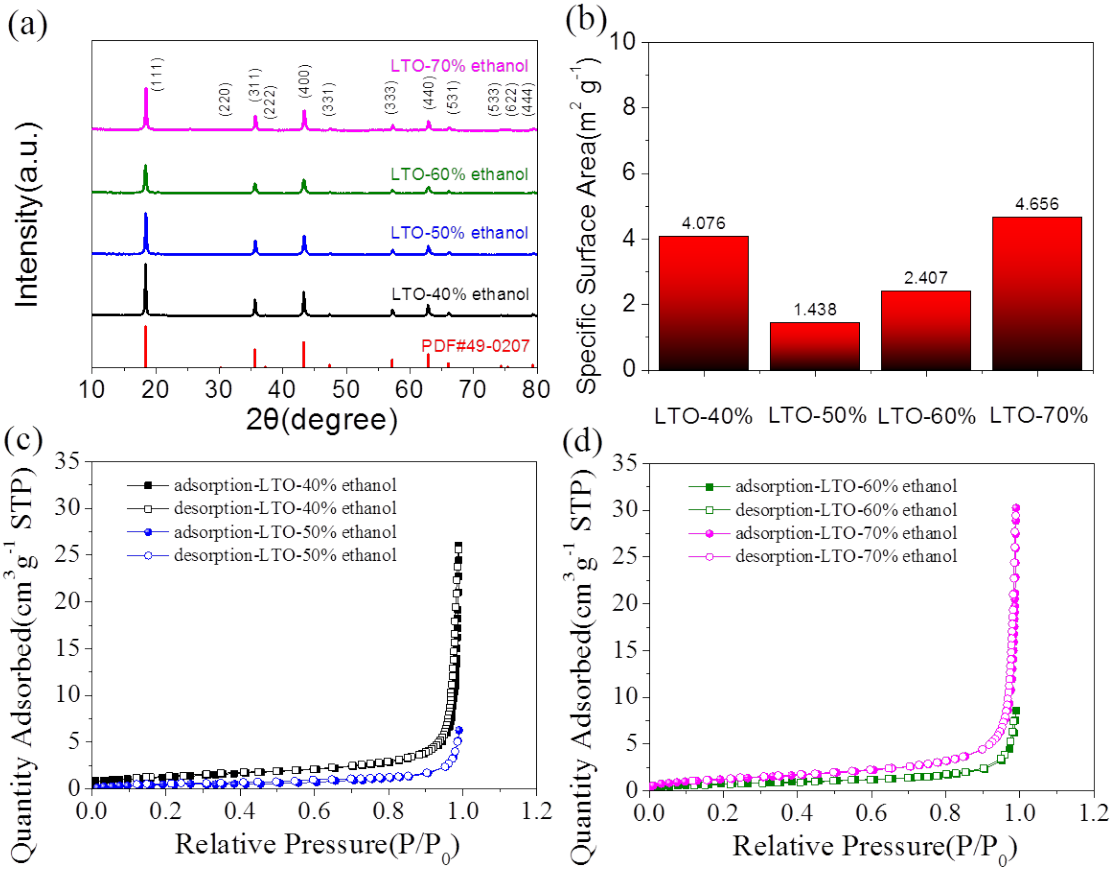

Fig. 1 (a) X-ray diffraction (XRD) patterns, (b) BET specific surface areas of LTO-40% ethanol, LTO-50% ethanol, LTO-60% ethanol and LTO-70% ethanol materials, (c, d) nitrogen adsorption/desorption isotherms at 77 K of LTO-40% ethanol, LTO-50% ethanol, LTO-60% ethanol and LTO-70% ethanol.

The compact LTO secondary microspheres were prepared using the TiN nanopowders, lithium acetate and glucose as precursor under the solution containing DI water and different ratio of ethanol. The XRD patterns of the as-prepared LTO materials with different ethanol proportion are shown in Fig. 1a, which are consistent with the JCPDS card No. 49-0207 and can be indexed to the spinel structure of LTO with the space group Fd3m[36]. The sharp peaks indicate the high crystalline of LTO materials. According to the Debye-Scherrer equation, the average size of primary nanograins for LTO-40% ethanol, LTO-50% ethanol, LTO-60% ethanol and LTO-70% ethanol materials is 53.3 nm, 39.8 nm, 27.2 nm and 44.7 nm,

respectively. The average size of primary grains for LTO-60% ethanol is much lower than that of other LTO samples, which leads to its lower the XRD peak intensity.

According to the nitrogen adsorption/desorption isotherms (Fig. 1c, d), it is found that these materials are nearly nonporous structure with only a small amount of micropore and mesopore. The specific surface area is mainly from the adsorption of the particle surface related with the particle size. The Brunauere-Emmette-Teller (BET) specific surface area of LTO-40% ethanol, LTO-50% ethanol, LTO-60% ethanol and LTO-70% ethanol are 4.07, 1.43, 2.40 and 4.65 $m^2 g^{-1}$ (Fig. 1b), respectively, which are much smaller than other reported nano-sized LTO materials of 178 and 46.4 $m^2 g^{-1}$ [15, 26]. The pore size distribution is obtained from the isotherm adsorption branches based on the Barrett–Joyner–Halenda (BJH) model. Their corresponding pore volumes are 0.039, 0.0094, 0.0124 and 0.045 $cm^3 g^{-1}$.The ultra-small BET specific surface areas and pore volumes demonstrate very dense structures of the LTO microspheres. This can obviously decrease the side reaction between LTO electrode and electrolyte, thereby attaining stable cycle performance. What's more, the LTO-50% ethanol and LTO-60% ethanol microspheres possess a high tap density of 1.34 and 1.23 g cm^{-3}, which is certainly in agreement with the really compact structure.

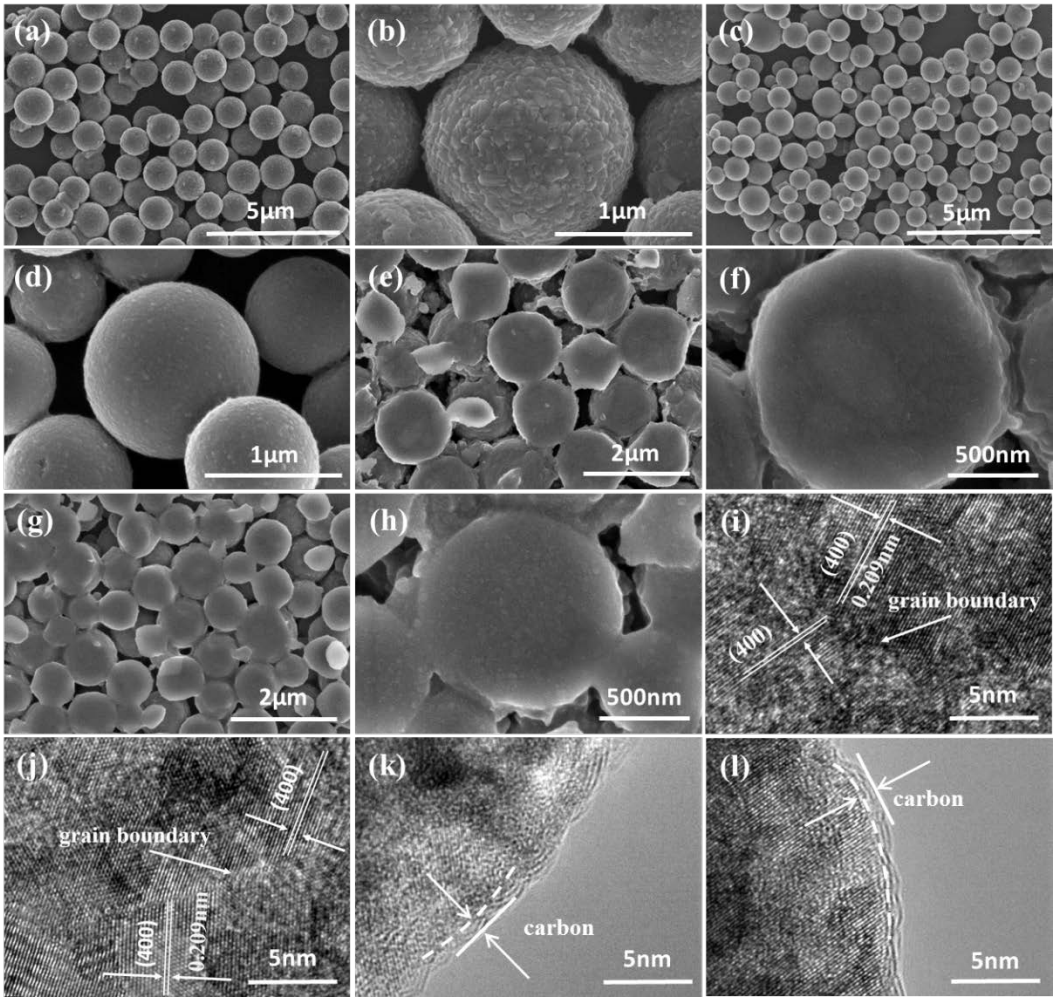

Fig. 2 SEM images of (a, b) LTO-50% ethanol and (c, d) LTO-60% ethanol; Cross-sectional SEM images of (e, f) LTO-50% ethanol and (g, h) LTO-60% ethanol microspheres; HRTEM images of (i, k) LTO-50% ethanol and (j, l) LTO-60% ethanol microspheres.

The scanning electron microscope (SEM) images of LTO microspheres are shown in Fig. 2. We can see that the LTO-40% ethanol consists of irregular spheres and particles with some nanoparticles and their aggregates (Fig. S1a, b). Whereas, the Fig. 2a, b shows that the LTO-50% ethanol presents uniform secondary microspheres with an average diameter of 1.4 μm, which consists of in-situ grown densely packed LTO nanocrystal. The compact structure are quite different from those previously reported secondary LTO materials with loosely packed structure[26]. When the ethanol proportion is further decreased to 60%, it is seen from Fig. 2c, d that densely packed LTO microspheres were also formed and their particle size is

in-homogenous and changes from 600 nm to 1.5 μm. In addition, the size of primary nanograins of LTO-60% ethanol is much smaller than that of LTO-50% ethanol, suggesting richer grain boundaries exist in LTO-60% ethanol. This result is corresponding to the calculation data using the Debye-Scherrer equation. The LTO compact structure results in high tap density, which can remarkably improve the volumetric energy density of battery. In sharp contrast, when the proportion of ethanol in the total solution is increased to 70%, the LTO-70% ethanol presents a quite different morphology as shown in Fig. S1c, d. This LTO material has a lamellar structure with a size range from 5 μm to 15 μm. At the same time, we note that the morphology of the precursor (Fig. S2) is nearly the same as the as-prepared LTO materials after annealing. The growth mechanism of these series of LTO materials can be described by the classical Lamer model [37]. The volume ratio of ethanol to total solution (R) plays significant role in the formation of the $Li_4Ti_5O_{12}$ materials, which may be due to following reasons: TiN nanopowders are gradually oxidized into Ti^{4+} and dissolved in water with the help of H_2O_2 and NH_3H_2O, after that the formed Ti^{4+} rapidly transforms to the Ti-peroxo complex $[Ti(OH)_3O_2]^-$ in the presence of H_2O_2 along with the formation of O_2 bubbles. The growth mechanism of LTO samples prepared with different amounts of ethanol can be analogously described by the classical Lamer model, which was originally introduced to explain the growth of monodisperse nanoparticles. Since the Ti-peroxo complex $[Ti(OH)_3O_2]^-$ is very soluble in water but hardly soluble in ethanol, different R values would bring about different solubilities of Ti-peroxo complex $[Ti(OH)_3O_2]^-$ in reaction solution for a given initial Ti species concentration. The $Li_4Ti_5O_{12}$ primary crystal is derived from the Ti-peroxo complex $[Ti(OH)_3O_2]^-$. Therefore, with increasing ethanol content, the saturation

concentration of Ti species in the reaction solution decreases, which results in different growth behaviors. Firstly, when the initial Ti species concentration (C) is just above the nucleation concentration (C_0) of Ti-peroxo complex $[Ti(OH)_3O_2]^-$, its discrete nucleation and growth can be maintained only for a short time. The C_0 would gradually decrease with increasing ethanol content, which leads to increase of the C-C_0 value as a driving force for the nucleation. As a result, the number of nucleation site increases and the size of the primary $Li_4Ti_5O_{12}$ nanograins decreases. This explains the effects of ethanol solvent amount on the texture properties of LTO-40%, LTO-50% and LTO-60% with a decrease of the average size of $Li_4Ti_5O_{12}$ nanograins. Secondly, when the R value increases to 70%, the initial Ti species concentration (C) is far above the nucleation concentration (C_0), resulting in more and continuous nucleation and further growth of the primary $Li_4Ti_5O_{12}$ nanograins to form LTO-70% with lamellar structure.

The cross-sectional SEM images of LTO-50% ethanol (Fig. 2e, f) and LTO-60% ethanol (Fig. 2g, h) further demonstrate that the as-prepared LTO microspheres are densely packed materials that consist of in-situ grown nanoparticles. There is no clear hole inside the spheres as shown in the high resolution SEM images (Fig. 2f, h). It is clearly seen from the TEM images in Fig. S3 that both LTO-50% ethanol and LTO-60% ethanol are not a porous structure but a solid structure, which is consistent with the BET results in Fig. 1b. The HRTEM images of LTO-50% ethanol in Fig. 2i show the well-defined crystalline structure with a lattice plane spacing of 0.209 nm corresponding with the (400) facet of spinel LTO. The nanocrystals inside the secondary spheres are tightly grown together to create abundant of grain boundaries, which may facilitate lithium ions transport inside the microspheres, while

no carbon coating is observed on the boundaries of nanocrystals. For the LTO-60% ethanol with much smaller primary particle size (Fig. 2j), there is quite richer grain boundaries throughout the microspheres. Under this situation, the abundant grain boundaries may also increase the intrinsic electrical conductivity and ionic conductivity, simultaneously[31]. This compact structure is corresponding to their high tap density. In addition, there is a uniform carbon layer on the LTO microspheres (Fig. 2k, l), and the thickness of carbon layer on LTO-50% ethanol and LTO-60% ethanol is 1-2 nm, which is probably arising from the glucose and results in the increase of electrical conductivity on the surface of microspheres. According to the thermogravimetric analysis (TGA), the content of amorphous carbon on LTO-50% ethanol and LTO-60% ethanol is 2.31% and 1.88%, respectively (Fig. S4). The uniform carbon layer can increase the surface electronic conductivity of the compact LTO spheres.

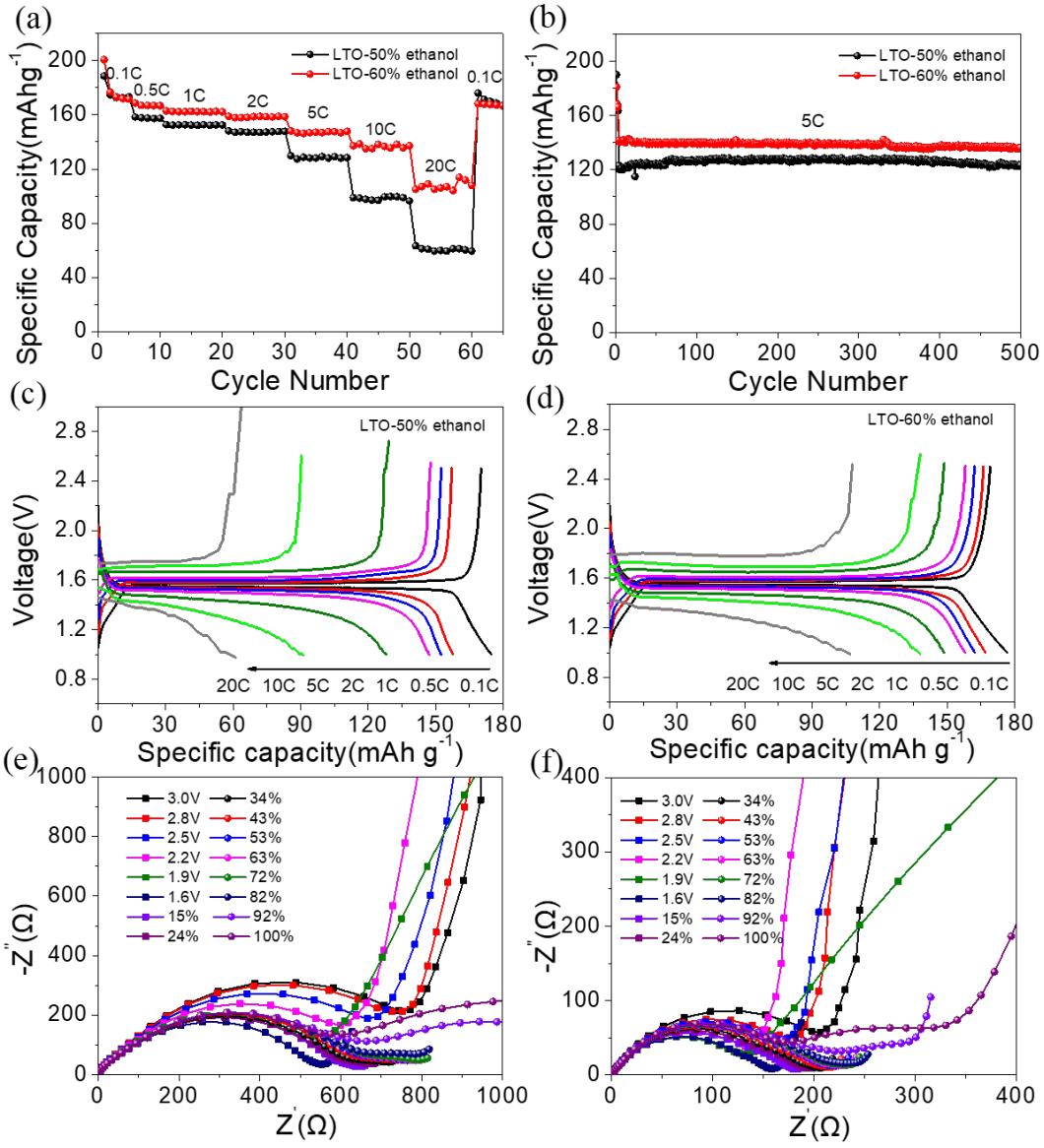

Fig. 3 Electrochemical properties of LTO microspheres: (a) specific capacities at different C rates, (b) cycle performance at a rate of 5 C, (c) (dis)charge curves of LTO-50% ethanol microspheres, (d) (dis)charge curves of LTO-60% ethanol microspheres. In-situ EIS spectra of (e) LTO-50% ethanol microspheres and (f) LTO-60% ethanol microspheres.

In order to identify the function of grain boundaries for the electrochemical properties, we tested the rate performance of this series of LTO materials. Fig. 3a shows the rate performance of the LTO materials at various charge/discharge rates of 0.1-20 C. At a low rate of 0.1 C, the LTO-60% ethanol delivers a remarkable specific capacity 0f 174.0 mA h g^{-1},

which is nearly the same as the theoretical capacity of 175 mA h g^{-1}. This microsphere also has a reversible discharge capacity of 166.7, 162.4, 158.8, 146.6 and 138.2 mA h g^{-1} at rates of 0.5 C, 1 C, 2 C, 5 C and 10 C, respectively. Even at a high rate of 20 C, the LTO-60% ethanol spheres still have a reversible discharge capacity of 111 mA h g^{-1}, exhibiting excellent rate performance, which is much larger than that of LTO-50% ethanol. For the compact LTO, the electrolyte is difficult to be infiltrated into the LTO, suggesting that the electron and ions depends on the solid transportation for the electrochemical reaction. The excellent high rate performance indicates that the compact LTO spheres have highly efficient electronic and ionic solid transportation. The rich grain boundary may provide three dimensional abundant channels for lithium ions. The cyclic voltammetry (CV) in Fig. S5 also show that the peak current density of LTO-60% ethanol is much higher than LTO-50% ethanol, reflecting the high kinetic properties resulting in faster electrochemical reaction of LTO-60% ethanol than LTO-50% ethanol. The much better rate performance of LTO-60% ethanol than LTO-50% ethanol indicates that particle size and grain boundary density have a significant effect on the electronic and ionic transportation. The smaller primary particles of LTO-60% ethanol generated more grain boundaries for highly efficient electronic and ionic solid transportation. It can be also found that the (dis)charge over-potentials for LTO-60% ethanol and LTO-50% ethanol is really small at 10 C and 20 C (Fig. 3c, d), which means the internal resistance for electron and lithium ions transport is rather small at high rates. In addition, both LTO-60% ethanol and LTO-50% ethanol present excellent high rate cycling performance (Fig. 3b). After 500 cycles at charge/discharge rate of 5 C, the capacity retention of LTO-60% ethanol and LTO-50% ethanol is as high as 97.8% and 96.7%. The outstanding cycle performance can

also be ascribed to the constant ionic and electronic transfer ability of grain boundaries. The LTO-40% ethanol and LTO-70% ethanol present relatively poor rate performance due to their limited Li-ion and electron transport ability as compared to that of LTO-60% (Fig. S6). Therefore, they may not meet the demand of combining a large volumetric energy density and power density simultaneously for lithium ion storage.

The kinetic behavior of LTO-50% ethanol and LTO-60% ethanol was further investigated using in-situ electrochemical impedance spectroscopy (EIS) (Fig. 3e, f**)**. As shown in Fig. 3e, f, the EIS consists of a depressed semicircle in high frequency regions corresponding to charge-transfer resistance (R_{ct}) and a slope line in low frequency regions related to Warburg impedance (Z_w), which exhibited the lithium ion diffusion in the microspheres[7, 38]. It can be clearly seen that the LTO-60% ethanol shows much smaller R_{ct} than LTO-50% ethanol at various state of charge (SOC). It is well-known that the R_{ct} is affected by both D_{Li} and the electronic conductivity, indicating that the more nanocrystals in compact LTO-60% ethanol sample constructs richer boundaries that can form more abundant 3D charge transport network for high efficient ionic and electronic transportation. The R_{ct} of both the LTO-50% ethanol and LTO-60% ethanol samples decreases from 15% SOC to 82% SOC as well as the initial lithiation process, which can be attributed to that the lithiation of grain boundary can further decreases the boundary resistance of LTO[31, 32]. The mobile lithium ions initially gather along the grain boundary where the lithium ion diffusivity increased dramatically as compared to the poor diffusivity of the $Li_4Ti_5O_{12}$ and $Li_7Ti_5O_{12}$ phase[12, 39]. CV and EIS results all demonstrate that the compact LTO microspheres presents high reaction kinetics arising from its abundant grain boundaries throughout the microspheres, which obviously improve

the Li-ion diffusion and transportation[31]. We have also summarized the electrochemical performance of other LTO anodes and our work (**Tables S1,** supporting information). It is seen that the as-prepared compact microspheres possess both excellent rate performance and high tap density.

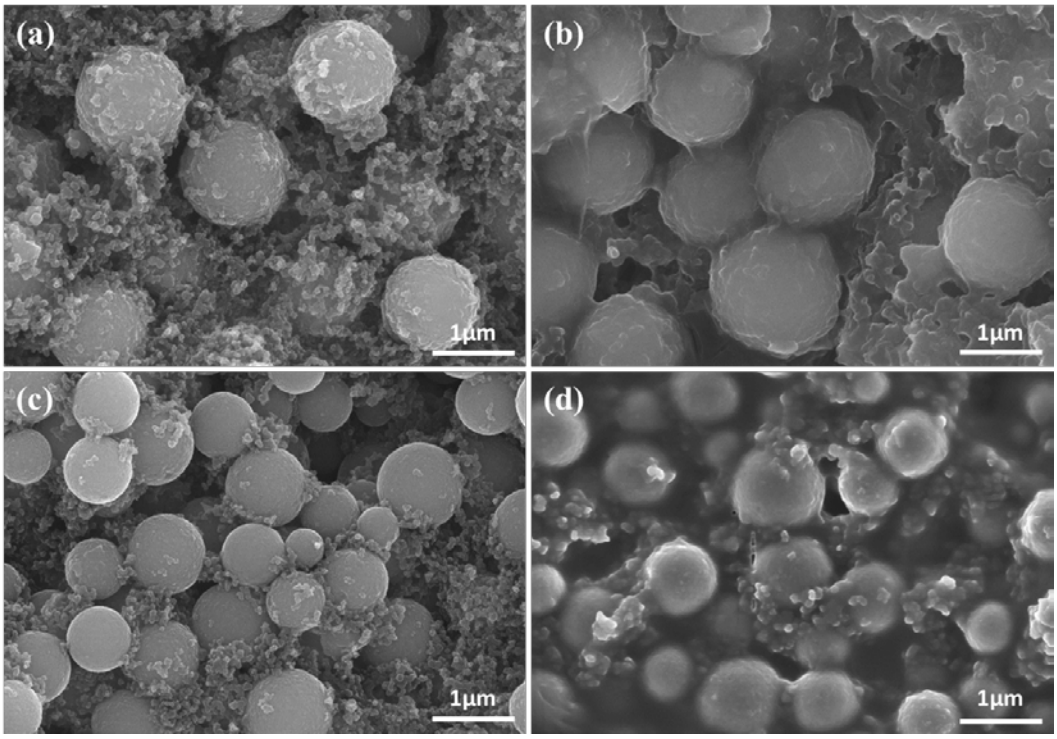

Fig. 4 SEM images of (a, b) LTO-50% ethanol and (c, d) LTO-60% ethanol before and after 500 cycles at 5C.

To examine the structure stability of LTO microspheres, SEM images before and after 500 cycles at 5C were also taken (Fig. 4). It is obviously that the LTO-50% ethanol and LTO-60% ethanol microspheres still keep their morphology and these spheres is rarely broken, which shows excellent structure stability. Furthermore, the in-situ XRD of LTO-60% ethanol and LTO-50% ethanol during charge/discharge is also adopted to prove their structure stability (Fig. S7)[40, 41]. Barely change of in-situ XRD patterns can be found, indicating high phase and

structure stability during the charge/discharge process at different rates. The excellent electrochemical performance and well maintained spherical morphology after cycling process of LTO-60% ethanol suggest that there is tiny side reaction due to its quite small surface area that barely influences its performance.

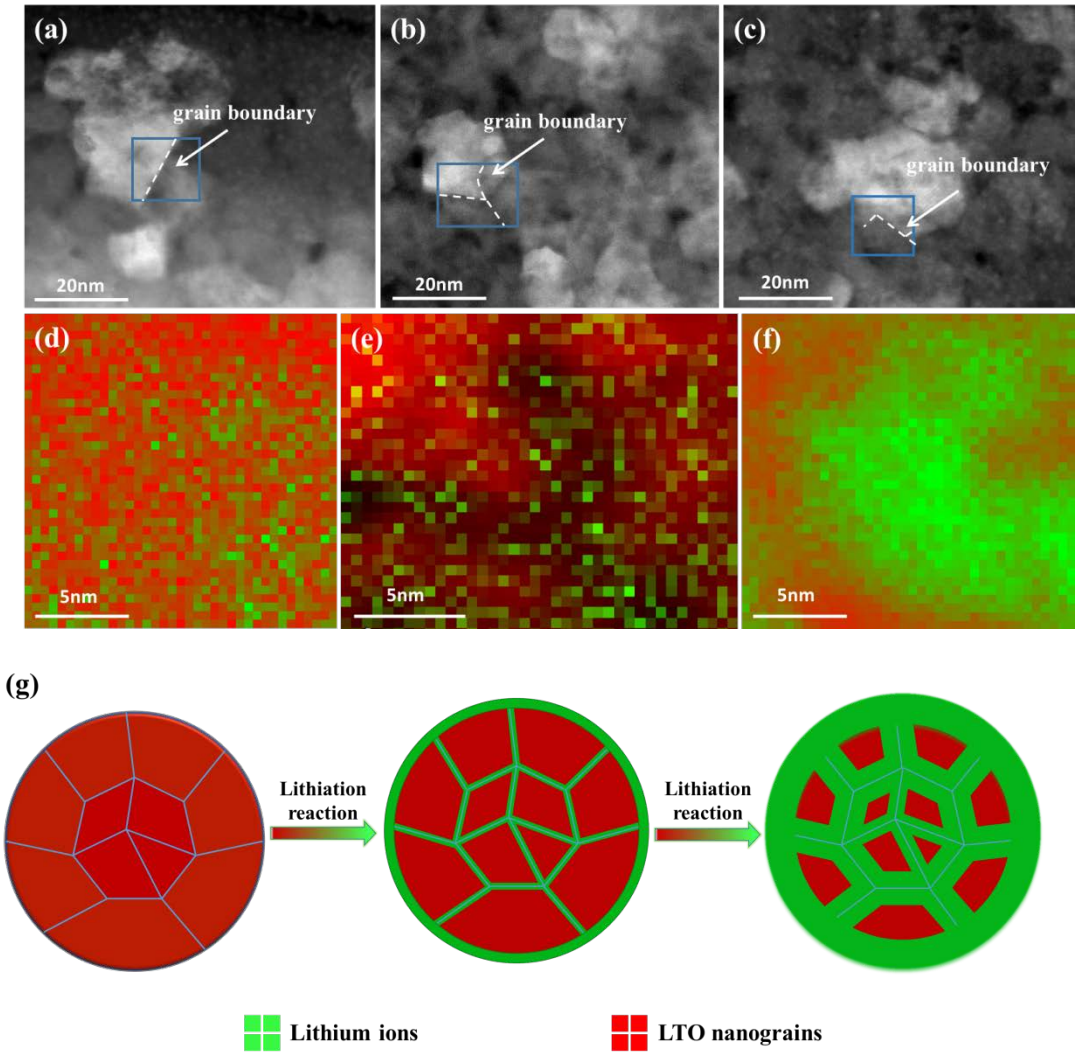

Fig. 5 STEM and EELS mapping images of LTO-60% ethanol microspheres at different SOC: 0% (pristine LTO) (a, d), 60% (b, e) and 80% (c, f), where the green points represent the lithium ions and red points is the LTO nanograins; (g) Schematic illustration of grain boundaries throughout the compact LTO microspheres and reaction mechanism of lithiation along grain boundaries.

To further reveal how the grain boundaries affect the lithium ion transportation and figure

out the reaction mechanisms with a real space observation in compact LTO secondary microspheres, the STEM-EELS mapping of LTO-60% ethanol with 0%SOC, 60% SOC and 80% SOC was adopted to observe the diffusion of the lithium ion around the boundaries (Fig. 5)[42]. The LTO electrode was discharged to 60% SOC and 80% SOC at 10C, and the EELS spectra of different SOC sample are shown in Fig. S8 in supporting information. All samples have a clear peak at around 61 eV corresponding to the Li-K edge energy-loss positions and the 80% SOC sample has the strongest peak intensity, suggesting more lithium ions in the selected area. Fig. 5a shows the STEM image of the pristine (0% SOC) LTO microspheres, which contains distinct grain boundaries. The STEM-EELS mapping demonstrates that lithium ions are uniformly distributed in the boundaries and primary crystals (Fig. 5a and Fig. 5d), suggesting that there is no lithium ion concentration difference at the grain boundaries and bulk LTO. When the LTO sample was discharged to 60% SOC at 10C, the STEM-EELS mapping presents that there is an obvious concentration difference of lithium ions between the grain boundary and bulk LTO (Fig. 5b and Fig. 5e). The lithium ions gather around the grain boundary instead of uniformly distributing among the whole 60% SOC sample. This phenomenon indicates that the LTO around the grain boundary was preferentially lithiated, suggesting that the grain boundaries have higher ability to transport lithium ions than bulk LTO during high rate lithiation[43]. The Ti^{4+} ions around the grain boundary were transformed to Ti^{3+} ions during lithiation of LTO that greatly enhanced the chemical reaction activity at grain boundary to form a $Li_7Ti_5O_{12}$ region[35], which benefits for the continuous Li ions and electrons transportation to achieve excellent rate performance. When LTO comes to a deeper lithium ions insertion process (80% SOC), the STEM-EELS mapping presents that the lithium

ion concentration at the grain boundary further increases and that in the bulk LTO also increases greatly (Fig. 5f), which presents an obvious gradient from grain boundary to bulk LTO. In order to distinguish the grain boundaries clearly, a higher magnification of STEM images are obtained as shown in Fig. S9 and the grain boundary can be clearly seen between bright region and dark region. We have also increased the scanning time of STEM-EELS to get more details in the mapping of 80% SOC sample. It can be found that there are more lithium ions around the grain boundaries. This result further demonstrates that the grain boundaries can achieve highly efficient lithium ion transportation, contributing to that the lithiation reaction of LTO are firstly initiated at grain boundaries and then diffused to bulk phase. Therefore, we conclude the reaction mechanism of these secondary microspheres as illustrated by Fig. 5g. Due to the availability of vacancies at grain boundaries leading to the facile diffusion through the lattice[44], it has more reactivity for lithium ions to intercalate the LTO lattice around the grain boundary regions as compared to bulk LTO and the grain boundaries provide faster lithium ion and electron transportation[45]. These abundant grain boundaries form a connecting ionic transportation network for highly efficient lithium ion transfer inside microspheres to achieve fast lithiation reaction from grain boundary to bulk LTO, which contribute to the excellent rate performance of the compact and high tap density LTO microspheres.

3. Conclusions

For fabricating the LTO materials which possess large tap densities, meanwhile barely compromising the charge transportation, we synthesized compact LTO secondary microspheres formed by densely packed LTO nanocrystals. The compact LTO secondary

microspheres have a high tap density of 1.23 g cm^{-3} along with an ultra-small specific surface area of 2.40 $m^2 g^{-1}$. The high tap density LTO microspheres show excellent long cycle and high rate performances. In addition, the LTO microspheres consisting of much smaller primary crystals and more abundant grain boundaries present better rate performance. The higher lithium-ion transportation ability of grain boundaries compared to bulk LTO are proved by STEM-EELS mapping. The grain boundaries in compact LTO microspheres can form a highly efficient and interconnected 3D channel for lithium-ion transportation. This work gives a real space distribution of lithium ions inside the compact LTO and revealed the function of grain boundaries for lithium ion transportation during high rate lithiation.

Supporting Information

Supporting Information is available from the Wiley Online Library or from the author.

Acknowledgements

This work was supported by the National Natural Science Foundation of China (51672156), Local Innovative Research Teams Project of Guangdong Pearl River Talents Program (No. 2017BT01N111), Guangdong special support program (2015TQ01N401), Guangdong Province Technical Plan Project (2017B010119001 and 2017B090907005), Shenzhen Technical Plan Project (JCYJ20170412170706047 and JCYJ20170817161221958).

Conflict of Interest

The authors declare no conflict of interest.

References

1. M. Armand and J.M. Tarascon, *Nature*, 2008**, 451**, 652-657.
2. M.V. Reddy, G.V. Subba Rao and B.V. Chowdari, *Chem. Rev.*, 2013**, 113**, 5364-5457.
3. B. Dunn and J.M. Tarascon, *Science*, 2011**, 334**, 928-935.
4. K.S. Park, A. Benayad, D.J. Kang and S.G. Doo, *J. Am. Chem. Soc.*, 2008**, 130**,

14930-14931.
5. X. Huang, H. Yu, J. Chen, Z. Lu, R. Yazami and H.H. Hng, *Adv. Mater.*, 2014**, 26**, 1295-1295.
6. L. Shen, H. Li, E. Uchaker, X. Zhang and G. Cao, *Nano Lett.*, 2012**, 12**, 5673-5678.
7. L. Tang, Y.-B. He, C. Wang, S. Wang, M. Wagemaker, B. Li, Q.-H. Yang and F. Kang, *Adv. Sci.*, 2017**, 4**, 1600311.
8. W.J.H. Borghols, M. Wagemaker, U. Lafont, E.M. Kelder and F.M. Mulder, *J. Am Chem. Soc.*, 2009**, 131**, 17786-17792.
9. J. Kim and J. Cho, *Electrochem. Solid St.*, 2014**, 10**, 84-101.
10. E. Kang, Y.S. Jung, G.H. Kim, J. Chun, U. Wiesner, A.C. Dillon, K.K. Jin and J. Lee, *Adv. Funct. Mater.*, 2011**, 21**, 4349–4357.
11. Y. Shi, L. Wen, F. Li and H.M. Cheng, *J. Power Sources.*, 2011**, 196**, 8610-8617.
12. W. Schmidt, P. Bottke, M. Sternad, P. Gollob, V. Hennige and M. Wilkening, *Chem. Mater.*, 2015**, 27**, 1740-1750.
13. M.R. Jo, K.M. Nam, Y. Lee, K. Song, J.T. Park and Y.M. Kang, *Chem. Commun.*, 2011**, 47**, 11474-11476.
14. L. Zhao, Y.S. Hu, H. Li, Z. Wang and L. Chen, *Adv. Mater.*, 2011**, 23**, 1385-1388.
15. C. Wang, S. Wang, L. Tang, Y.B. He, L. Gan, J. Li, H. Du, B. Li, Z. Lin and F. Kang, *Nano Energy*, 2016**, 21**, 133-144.
16. B. Li, C. Han, Y.B. He, C. Yang, H. Du, Q.H. Yang and F. Kang, *Energ. Environ. Sci.*, 2012**, 5**, 9595-9602.
17. C. Han, Y.B. He, H. Li, B. Li, H. Du, X. Qin and F. Kang, *Electrochim. Acta.*, 2015**, 157**, 266-273.
18. Y. He, B. Li, M. Liu, C. Zhang, W. Lv, C. Yang, J. Li, H. Du, B. Zhang and Q. Yang, *Sci. Rep-Uk.*, 2012**, 2**, 913.
19. Z. Yao, X. Xia, C.A. Zhou, Y. Zhong, Y. Wang, S. Deng, W. Wang, X. Wang and J. Tu, *Adv. Sci.*, 2018**, 5**, 1700786.
20. H. Lu, J. Hagberg, G. Lindbergh and A. Cornell, *Nano Energy*, 2017**, 39**, 140-150.
21. Z. Yao, X. Xia, Y. Zhong, Y. Wang, B. Zhang, D. Xie, X. Wang, J. Tu, Y. Huang and Z. Yao, *J. Mater. Chem. A.*, 2017**, 5**, 8916-8921.
22. L. Shen, X. Zhang, E. Uchaker, C. Yuan and G. Cao, *Adv. Energy Mater.*, 2012**, 2**, 691-698.
23. J. Kim, K.E. Lee, K.H. Kim, S. Wi, S. Lee, S. Nam, C. Kim, O.K. Sang and B. Park, *Carbon*, 2017**, 114**, 275-283.
24. M. Odziomek, F. Chaput, A. Rutkowska, Ś. K, D. Olszewska, M. Sitarz, F. Lerouge and S. Parola, *Nat. Commun.*, 2017**, 8**, 15636.
25. S.Y. Han, I.Y. Kim and S.J. Hwang, *J. Phys. Chem. Solids.*, 2012**, 73**, 1444-1447.
26. Y. He, A. Muhetaer, J. Li, F. Wang, C. Liu, Q. Li and D. Xu, *Adv. Energy Mater.*, 2017**, 7**, 1700950.

27. J.G. Kim, D. Shi, M.S. Park, G. Jeong, Y.U. Heo, M. Seo, Y.J. Kim, J.H. Kim and S.X. Dou, *Nano Res.*, 2013**, 6**, 365-372.
28. Z. Zhang, G. Li, H. Peng and K. Chen, *J. Mater. Chem. A.*, 2013**, 1**, 15429-15434.
29. J. Liu, K. Song, P.A. van Aken, J. Maier and Y. Yu, *Nano Lett.*, 2014**, 14**, 2597-2603.
30. T. Yuan, Z. Tan, C. Ma, J. Yang, Z.F. Ma and S. Zheng, *Adv. Energy Mater.*, 2017**, 7**, 1601625.
31. C. Wang, S. Wang, Y.B. He, L. Tang, C. Han, C. Yang, M. Wagemaker, B. Li, Q.H. Yang and J.K. Kim, *Chem. Mater.*, 2015**, 27**, 5647-5656.
32. W. Schmidt and M. Wilkening, *J. Phys. Chem. C.*, 2016**, 120**, 1861-1871.
33. M. Kitta, T. Akita, S. Tanaka and M. Kohyama, *J. Power Sources.*, 2013**, 237**, 26-32.
34. M. Kitta, T. Akita, S. Tanaka and M. Kohyama, *J. Power Sources.*, 2014**, 257**, 120-125.
35. K. M and K. M, *Phys. Chem. Chem. Phys.*, 2017**, 19**, 11581-11587.
36. S. Scharner, W. Weppner and P. Schmid-Beurmann, *J. Electrochem. Soc.*, 1999**, 146**, 857-861.
37. S. Wang, Y. Ding, S. Xu, Y. Zhang, G. Li, L. Hu and S. Dai, *Chem. Eur. J.*, 2014**, 20**, 4916-4920.
38. Y.B. He, M. Liu, Z.D. Huang, B. Zhang, Y. Yu, B. Li, F. Kang and J.K. Kim, *J. Power Sources.*, 2013**, 239**, 269-276.
39. M. Wilkening, R. Amade, W. Iwaniak and P. Heitjans, *Phys. Chem. Chem. Phys.*, 2007**, 9**, 1239-1246.
40. F. Ronci, P. Reale, A. B. Scrosati, S. Panero,V.R.A. And, P. Perfetti, M.D.M. And and J.M. Merino, *J. Phys. Chem. B.*, 2002**, 106**, 3082-3086.
41. M. Wagemaker, D.R. Simon, E.M. Kelder, J. Schoonman, C. Ringpfeil, U. Haake, D. Lützenkirchen‐Hecht, R. Frahm and F.M. Mulder, *Adv. Mater.*, 2010**, 18**, 3169-3173.
42. M. Kitta, T. Akita and M. Kohyama, *J. Electrochem. Soc.*, 2015**, 162**, A1272-A1275.
43. M.M. Rahman, J.Z. Wang, M.F. Hassan, D. Wexler and H.K. Liu, *Adv. Energy Mater.*, 2011**, 1**, 212-220.
44. M. Wagemaker, E.R.H.V. Eck, A.P.M. Kentgens and F.M. Mulder, *J. Phys. Chem. B.*, 2009**, 113**, 224-230.
45. C. Kim, N.S. Norberg, C.T. Alexander, R. Kostecki and J. Cabana, *Adv. Funct. Mater.*, 2013**, 23**, 1099-1099.

TOC Graphic

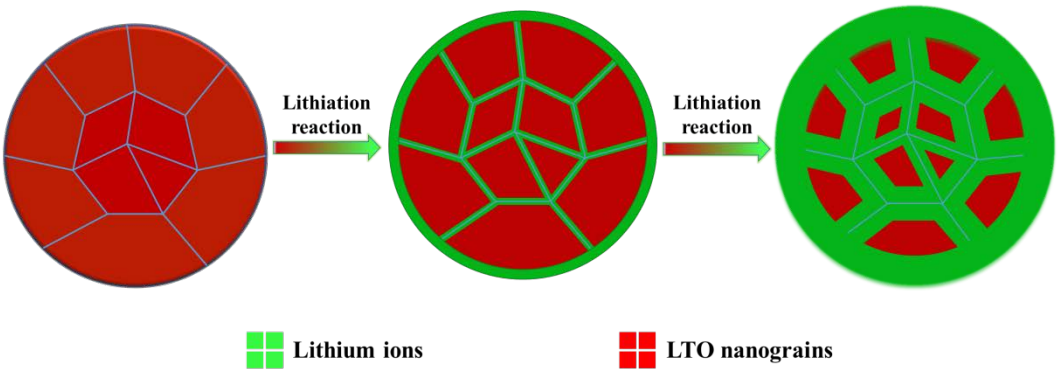

Lithium ions LTO nanograins